Eur. Phys. J. C (2024) 84:1180
https://doi.org/10.1140/epjc/s10052-024-13491-1

THE EUROPEAN PHYSICAL JOURNAL C

Regular Article

Theoretical Physics

Hamiltonian formulation of relativistic magnetohydrodynamic accretion on a general spherically symmetric and static black hole: quantum effects on shock states

Mustapha Azreg-Aïnou[1,a], **Mubasher Jamil**[2,b], **Sousuke Noda**[3,c]

[1] Engineering Faculty, Bağlica Campus, Başkent University, 06790 Ankara, Turkey
[2] School of Natural Sciences, National University of Sciences and Technology, H-12, Islamabad 44000, Pakistan
[3] Miyakonojo College, National Institute of Technology, Miyakonojo 885-8567, Japan

Received: 9 August 2024 / Accepted: 12 October 2024 / Published online: 19 November 2024

Abstract In this paper, our aim is to extend our earlier work [Ahmed et al. in Eur. Phys. J. C 76:280, 2016], investigating an axisymmetric plasma flow with angular momentum onto a spherical black hole. To accomplish that goal, we focus on the case in which the ideal magnetohydrodynamic approximation is valid, utilizing certain conservation laws which arise from particular symmetries of the system. After formulating a Hamiltonian of the physical system, we solve the Hamilton equations and look for critical solutions of (both in and out) flows. Reflecting the difference from the Schwarzschild spacetime, the positions of sonic points (fast magnetosonic point, slow magnetosonic point, Alfvén point) are altered. We explore several kinds of flows including critical, non-critical, global, magnetically arrested and shock induced. Lastly, we analyze the shock states near a specific quantum corrected Schwarzschild black hole and determine that quantum effects do not favor shock states by pushing the shock location outward.

1 Introduction

Black holes are one of the enduring predictions of Einstein's theory of general relativity (GR). For more than 50 years after GR was proposed, black holes (BHs) remained a mathematical curiosity, which led theorists to find several new BH solutions by solving Einstein's field equations and a few basic gravitational collapse models [1]. However, in the 1970s and 1980s, there first appeared empirical evidence for the existence of stellar mass BHs with the observations of the Cygnus X-1 binary system [2–4]. Further, the detection and controversy of mysterious quasars in the 1960s led to the idea of supermassive black holes due to their ultra-compactness and super-luminous characteristics [5]. In the last few years, more direct evidence favoring the existence of both intermediate and supermassive BHs has been gathered using the observations of gravitational waves associated with the merger of BHs by the LIGO/Virgo Collaboration [6], as well as the detection of shadows of supermassive BHs at the center of the M87 [7] and Milky Way [8] galaxies by the Event Horizon Telescope (EHT) Collaboration. These discoveries have given rise to phenomenological studies testing black hole solutions in different modified gravity theories for constraining the arbitrary parameters of the spacetime metric and the underlying theory.

Historically, the simplest model of accretion of matter on a stellar body was studied by Bondi, mainly considering the accretion flow governed by Newtonian laws [9]. Later, this model was extended by Michel to consider steady-state hydrodynamic accretion, with the fluid having a polytropic equation of state. In this model, the fluid flow admits a transonic solution [10]. Based on Michel's model of spherical and steady-state accretion, other authors have made numerous extensions by considering axisymmetric flows as well as accretion of exotic matter, which includes dark matter and dark energy [11–13]. Numerous models of accretion on black holes exist in the literature; for a review see [14]. We proposed a model of spherical accretion of an ideal fluid for spherically symmetric black holes, modeling the system as a dynamical system in a plane (r, v), where r is the radial coordinate and v is the three-dimensional speed of the fluid [15], which has been further explored by other authors as

[a] e-mail: azreg@baskent.edu.tr
[b] e-mail: mjamil@sns.nust.edu.pk (corresponding author)
[c] e-mail: snoda@cc.miyakonojo-nct.ac.jp

well [16–20]. By solving the Hamilton equations, we determined the sonic points (also known as critical points) and non-sonic critical points for ordinary fluids and fluids with exotic equations of state. We explored the implications of isothermal and polytropic fluids for spherical accretion. In this article, we are interested in extending our previous work for the magnetohydrodynamic (MHD) inflow towards spherically symmetric black holes.

The motivation for pursuing the present investigation arises from an exciting discovery made by the EHT. In 2021, the EHT team imaged polarized emission around the supermassive BH in M87 on event horizon scales. This synchrotron polarized emission probed the underlying structure of the magnetic fields and plasma near the BH. The EHT team reported the average number density $n_e \sim 10^{4-7}\mathrm{cm}^{-3}$, magnetic field strength $B \sim 1$–30 G, and electron temperature $T_e \sim 10^{10}$K [21]. Their model predicted that the M87 central black hole has a mass accretion rate of (3–20) $\times 10^{-4} M_{\odot}\mathrm{year}^{-1}$. This observation clearly suggests that the M87* BH accretes magnetized plasma whose dynamics are governed by both gravitational and magnetic fields. It is no surprise, though, that large supermassive black holes like M87* have small magnetic fields, and vice versa, due to the inverse relationship between the BH gravitational radius and the magnetic field strength [22]. As a consequence, BHs larger than 10^{10} solar mass are undetectable and remain in obscurity. Separate studies in the literature dealing with BH shadows explore the effects of magnetized and non-magnetized plasmas on the geometry of the BH shadow [23–25]. These studies reveal that the shadow radius is altered due to plasma effects, and may increase or decrease by adjusting the model free parameters. In addition, it has been noted that strong magnetized plasma regions near the black holes are formed as a result of shocks in MHD plasma [26]; hence, shock generation should be investigated alongside the accretion mechanism of black holes.

Several models of general relativistic MHD accretion for black holes have been investigated in the literature, with assumptions including ideal MHD and advective and viscous systems [27,28]. The MHD flow into a Schwarzschild black hole is discussed in [29] by solving the Grad–Shafranov equation. This equation describes the interaction between the frozen-in plasma and the surrounding global magnetic field. For the Kerr case, solving the Grad–Shafranov equation is much more difficult; therefore, the poloidal structure of the magnetosphere, which corresponds to the shape of the magnetic surface (equivalently given stream function $\Psi(r, \theta)$) is given by hand. In [30], the authors assumed the stream function, and fluid flow along the streamline was investigated. In this paper, instead of assuming the shape of the magnetic surface, we consider an axisymmetric inflow restricted in a plane around the black hole by fixing the value of an angular coordinate, which is similar to the analysis of inflow on the equatorial plane of a Kerr black hole [31].

This paper is structured as follows: In Sect. 2, we present the governing equations of accretion of plasma on a general static and spherical black hole, along with the symmetries of the model and the corresponding conservation laws. Section 3 deals with the solution of the governing equations utilizing the conservation laws. In particular, we determine the Hamiltonian of our system, determine the fluid velocity components, and solve the Hamilton equations to find the critical points as well. As a special case, we analyze the accretion model of the polytropic fluid. In Sect. 4, we study a special model of spherical MHD accretion on a Schwarzschild black hole and present the conditions under which inflow or outflow can occur in the vicinity of the black hole. Here, we explore several kinds of flows including critical, global, and magnetically arrested, and shocks in flows. Lastly, we analyze the shock states near the quantum-corrected Schwarzschild black hole. Throughout, we work in the units $c = G_N = \hbar = 1$, unless otherwise noted.

2 Magnetohydrodynamics in the spherical black hole spacetime

As the background spacetime, we consider a static and spherical black hole with (or without) quantum correction, of which the general form of the metric is given as

$$\mathrm{d}s^2 = g_{tt}(r)\mathrm{d}t^2 + g_{rr}(r)\mathrm{d}r^2 + g_{\theta\theta}(r)(\mathrm{d}\theta^2 + \sin^2\theta\mathrm{d}\varphi^2), \tag{1}$$

where the components of the metric are functions of the coordinate r, which depends on gravitational theories, quantum correction, and so on. Here, we do not assume the functional form yet, but when deriving MHD flow solutions, we shall consider one kind of spherical black hole.

Now, we introduce the magnetohydrodynamics in curved spacetime, endowed with spherical symmetry within the ideal MHD approximation that the conductivity of the fluid tends to infinity, implying a vanishing electric field for a comoving observer: $F_{\mu\nu}u^\nu = F^{\mu\nu}u_\nu = 0$, where u^μ is the four-velocity of flow satisfying $u_\mu u^\mu = -1$. We apply the method introduced in the pioneering papers [30,32–36]. Under these assumptions, we investigate the ideal MHD steady and advective inflow onto a spherically symmetric black hole. The MHD flow is governed by three conserved laws (namely, the particle number conservation, the energy conservation, and the angular momentum conservation), the Maxwell equation, and the ideal MHD condition, respectively: [14]

$$\nabla_\mu(nu^\mu) = 0, \tag{2}$$

$$\nabla_\mu(-T^\mu{}_\nu k^\nu) = 0, \tag{3}$$
$$\nabla_\mu(T^\mu{}_\nu m^\nu) = 0, \tag{4}$$
$$\nabla_\mu {}^*F^{\mu\nu} = 0, \tag{5}$$
$$F^{\mu\nu}u_\nu = 0, \tag{6}$$

where n is the proper particle number density, k^μ and m^μ are Killing vectors $k^\mu = (1, 0, 0, 0)$ and $m^\mu = (0, 0, 0, 1)$, ${}^*F^{\mu\nu}$ is the dual to $F^{\mu\nu}$, and $T^{\mu\nu}$ is the energy momentum tensor

$$T^{\mu\nu} = (\rho + p)u^\mu u^\nu + pg^{\mu\nu} + \frac{1}{4\pi}\left(F^{\mu\alpha}F^\nu_\alpha - \frac{1}{4}g^{\mu\nu}F^{\alpha\beta}F_{\alpha\beta}\right), \tag{7}$$

which consists of the plasma part with the total energy density of plasma gas ρ and its pressure p, and the electromagnetic field part.

From now on we assume that the plasma is confined in a narrow (thin) accretion disk located in the equatorial plane $\theta = \pi/2$ in such a way that the component u^θ of the velocity vector is taken to be null (i.e., the matter from the accretion disk does not leave the equatorial plane throughout the motion). As we shall see below, this implies $B^\theta = 0$. The plasma is distributed symmetrically about the black hole (hereafter BH) and the inflow is assumed to be axisymmetric and stationary. Under this assumption, the electromagnetic (EM) field acquires axial symmetry about the z-axis around which the plasma is revolving. In this paper, we investigate two different outer boundary conditions separately: the first one concerns in-falling matter starting its motion from the outer edge $r = r_{\rm edge}$ on the equatorial plane of the BH with negligible radial velocity, as shown in Fig. 1, while the second boundary is the case of accretion of the wind from a companion object, for which the radial flow velocity at the outer edge may be so fast that it is initially supersonic.

For the stationary and axisymmetric EM field, the Lie derivative of the EM field tensor is zero: $\mathcal{L}_{\rm k}F_{\alpha\beta} = 0$, $\mathcal{L}_{\rm m}F_{\alpha\beta} = 0$, where $\rm k = k^\mu\partial_\mu$ and $\rm m = m^\mu\partial_\mu$ are Killing vectors. In the coordinates (t, r, θ, φ) describing the metric, the Lie derivatives for the EM field tensor become respectively

$$F_{\alpha\beta,t} = 0, \quad F_{\alpha\beta,\varphi} = 0. \tag{8}$$

Together, one of the Maxwell equations $F_{[\alpha\beta;\gamma]} = F_{[\alpha\beta,\gamma]} = 0$, and (8) yield

$$F_{t\varphi,r} = 0, \quad F_{t\varphi,\theta} = 0. \tag{9}$$

Therefore, the $t\varphi$-component of the field strength satisfies $F_{t\varphi,\mu} = 0$, and equivalently, $F_{t\varphi} = \text{const}$. We can choose this constant to be zero by imposing some appropriate asymptotic conditions. Hence,

$$F_{t\varphi} = 0. \tag{10}$$

Using this along with (6) and the symmetry constraints $u^\theta = 0$[1] and the fact that no EM field depends on (t, φ) coordinates, then the Maxwell equations $F_{[\alpha\beta;\gamma]} = F_{[\alpha\beta,\gamma]} = 0$, yield $F_{tr} = F_{\varphi r} = 0$. For stationary and axisymmetric MHD flow, these same symmetry constraints yield the following conservation laws, where Ω_F and η are constants along each flow line (i.e., $\mathrm{d}\Omega_F/\mathrm{d}\tau = 0$ and $\mathrm{d}\eta/\mathrm{d}\tau = 0$) [32]:

$$\Omega_F := -\frac{F_{t\theta}}{F_{\varphi\theta}}, \quad \frac{F_{\varphi\theta}}{\sqrt{-g}nu^r} := -\frac{1}{\eta}, \quad \frac{F_{r\theta}}{\sqrt{-g}n(u^\varphi + \Omega_F u^t)} = \frac{1}{\eta}. \tag{11}$$

Note that $F_{tr} = F_{\varphi r} = 0$ because of the constraint $u^\theta = 0$; this is to say that in the limit $u^\theta \to 0$, we have $F_{tr} \to 0$ and $F_{\varphi r} \to 0$, but $F_{tr}/F_{\varphi r} = \Omega_F$ [32]. On combining the equations given in (11), we obtain

$$F_{r\theta}\,\dot{r} = F_{\varphi\theta}(\Omega_F - \Omega), \tag{12}$$

which can be derived directly from the ideal MHD condition (6). Here, $\dot{r} \equiv \mathrm{d}r/\mathrm{d}t$, $\Omega \equiv u^\varphi/u^t = \dot{\varphi}$ is the angular velocity of the plasma flow, and Ω_F is the angular frequency of the streamline, which is constant along each flow line, manifesting the well-known line isorotation law.

The mass conservation law (2) becomes $\partial_r(\sqrt{-g}nu^r) = 0$ due to the symmetry assumptions. This implies

$$\sqrt{-g}nu^r = \text{const} = C, \quad \text{for all } r, \tag{13}$$

where C denotes the BH accretion rate.

Using the above conserved quantities, the field strength can be written in terms of the flow velocities as

$$F_{\mu\nu} = \begin{pmatrix} 0 & 0 & F_{t\theta} & 0 \\ & 0 & F_{r\theta} & 0 \\ & & 0 & F_{\theta\varphi} \\ & & & 0 \end{pmatrix} = \frac{\sqrt{-g}\,n}{\eta}\begin{pmatrix} 0 & 0 & \Omega_F u^r & 0 \\ & 0 & u^\varphi + \Omega_F u^t & 0 \\ & & 0 & u^r \\ & & & 0 \end{pmatrix}. \tag{14}$$

The expression of the magnetic field, measured in a laboratory frame, is defined by $B_\mu = -\eta_{\mu\nu\alpha\beta}k^\nu F^{\alpha\beta}/2$, where $\eta_{\mu\nu\alpha\beta} = \sqrt{-g}\,\epsilon_{\mu\nu\alpha\beta}$ $(\epsilon_{tr\theta\varphi} = +1)$. As we noted earlier, $F_{tr} = F_{\varphi r} = 0$, because of the constraint $u^\theta = 0$; now, inserting $F_{\varphi r} = 0$ into the expression of B_μ yields $B_\theta = B^\theta = 0$. Introducing the poloidal magnetic field B and the poloidal velocity of fluid u by $B^2 := (B_r B^r + B_\theta B^\theta)/g_{tt}^2 = -(F_{\theta\varphi})^2/(g_{tt}g_{\varphi\varphi}^2)$ and $u^2 := u_r u^r + u_\theta u^\theta = g_{rr}(u^r)^2$, we

[1] The assumption $u^\theta = 0$ has an important consequence: It implies that any quantity that is conserved on each flow line is conserved for all r. In fact, since partial derivatives of all fields with respect to t and φ are zero, the relation $d(.)/\mathrm{d}\tau = 0$, where (.) represents any quantity that is conserved on each flow line as Ω_F and η, implies that $d(.)/\mathrm{d}\tau = u^\alpha(.)_{,\alpha} = u^r(.)_{,r} = 0$, and thus $(.)_{,r} = 0$.

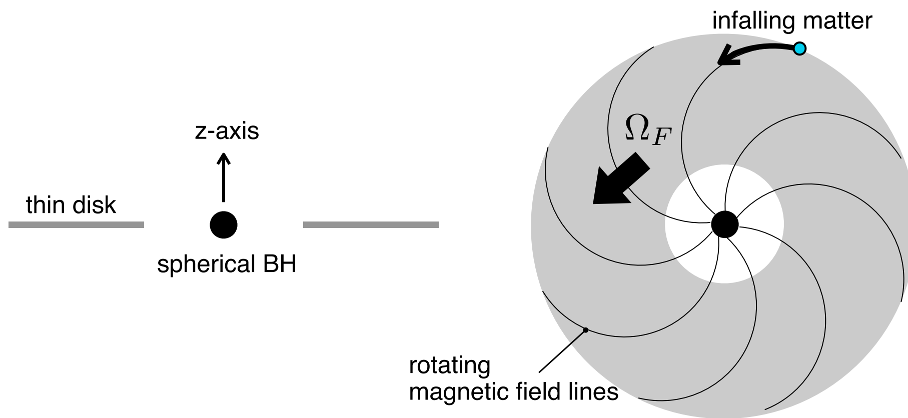

Fig. 1 Schematic of an in-falling plasma: the left and right panels depict the views of the present inflow from the edge-on direction and from the z-axis, respectively. The matter starts from the outer edge of the thin accretion disk

see that η given in (11) reduces to

$$|\eta| = \left|\frac{\sqrt{-g}\, nu^r}{F_{\theta\varphi}}\right| = \left|\sqrt{-g_{tt}g_{rr}}\, g_{\varphi\varphi}\frac{nu^r}{F_{\theta\varphi}}\right| = \left|n\frac{u}{B}\right|, \quad (15)$$

and represents the particle flux per unit flux-tube [30] or the mass flux per unit poloidal magnetic field.

In addition to Ω_F and η, we also have $\mathcal{E}$ and $\mathcal{L}$, which correspond to energy and angular momentum. The conservation laws (3) and (4) yield

$$\partial_r\left(-\sqrt{-g}T^r{}_t\right) = 0, \quad \partial_r\left(\sqrt{-g}T^r{}_\varphi\right) = 0, \quad (16)$$

respectively. Therefore, we can introduce the following conserved quantities:

$$\begin{aligned}\mathcal{E} &:= \frac{-\sqrt{-g}T^r{}_t}{F_{\theta\varphi}\eta} = -\frac{\sqrt{-g}}{F_{\theta\varphi}\eta}\\ &\quad\times\left[(\rho+p)u^r u_t + \frac{g^{rr}g^{\theta\theta}}{4\pi}F_{r\theta}F_{t\theta}\right]\\ &= -hu_t - \frac{B_\varphi}{4\pi\eta}\Omega_F, \quad (17)\end{aligned}$$

$$\begin{aligned}\mathcal{L} &:= \frac{\sqrt{-g}T^r{}_\varphi}{F_{\theta\varphi}\eta} = \frac{\sqrt{-g}}{F_{\theta\varphi}\eta}\\ &\quad\times\left[(\rho+p)u^r u_\varphi + \frac{g^{rr}g^{\theta\theta}}{4\pi}F_{r\theta}F_{\varphi\theta}\right] = hu_\varphi - \frac{B_\varphi}{4\pi\eta}, \quad (18)\end{aligned}$$

where h is the specific enthalpy defined as

$h := (\rho+p)/n$. Note that since $F_{\theta\varphi}\eta = -\sqrt{-g}nu^r$ given in (11) is conserved for all r, the quantities $\mathcal{E}$ and $\mathcal{L}$ are also conserved for all r.

There are two remaining constants of motion, Φ_1, Φ_2, which can be related to C, Ω_F, η as follows. The $t-$ and $\varphi-$ source-free equations (5) yield

$$\begin{aligned}\Phi_1 &= -\sqrt{-g}(u^t b^r - u^r b^t),\\ \Phi_2 &= \sqrt{-g}(u^r b^\varphi - u^\varphi b^r), \quad (19)\end{aligned}$$

where b^μ is the magnetic field in the fluid frame

$$b_\mu = -\frac{1}{2}\eta_{\mu\nu\alpha\beta}u^\nu F^{\alpha\beta}. \quad (20)$$

It is then straightforward to show that

$$\Omega_F = \frac{\Phi_2}{\Phi_1}, \quad \eta = -\frac{C}{\Phi_1}. \quad (21)$$

3 Flow solutions

To obtain flow solutions, we introduce kinematic variables describing the ideal MHD flow. Due to the symmetry in the present case, the system can be represented by a Hamiltonian that is a function of two variables, namely, position of fluid parcel r and its velocity V. Moreover, using a property of the Hamiltonian, we obtain the so-called wind equation, giving critical points (CPs).

3.1 Kinematic variables of the flow

Using (12) and the definition of η, the azimuthal component of the magnetic field $B_\varphi = \sqrt{-g}F^{r\theta}$ can be written in terms of u_t and u_φ as

$$\begin{aligned}B_\varphi &= g^{rr}g^{\theta\theta}\sqrt{-g}\frac{F_{\theta\varphi}}{u^r}(u^\varphi - \Omega_F u^t)\\ &= -gg^{rr}g^{\theta\theta}\frac{n}{\eta}(u^\varphi - \Omega_F u^t)\\ &= -\frac{n}{\eta}(g_{tt}u_\varphi - \Omega_F g_{\varphi\varphi}u_t). \quad (22)\end{aligned}$$

Substituting this into (17) and (18), we obtain

$$\mathcal{E} = -\left(h + \frac{n}{4\pi\eta^2}\Omega_F^2 g_{\varphi\varphi}\right)u_t + \frac{n}{4\pi\eta^2}\Omega_F g_{tt}u_\varphi, \quad (23)$$

$$\mathcal{L} = -\frac{n}{4\pi\eta^2}\Omega_F g_{\varphi\varphi}u_t + \left(h + \frac{n}{4\pi\eta^2}g_{tt}\right)u_\varphi. \quad (24)$$

To determine the CPs and the profile of the flow, we will not integrate the set of differential equations governing the flow; rather, we will apply a Hamiltonian approach like we used earlier in [15,17,20,37]. In the $(\theta = \pi/2)$-plane, rewriting (1) as $ds^2 = -(\sqrt{-g_{tt}}dt)^2 + (\sqrt{g_{rr}}dr)^2 + (\sqrt{g_{\varphi\varphi}}\mathrm{d}\varphi^2)$, we see that the three-velocity components are

$$v_r = \frac{\sqrt{g_{rr}}}{\sqrt{-g_{tt}}}\,\dot{r}, \quad v_\varphi = \frac{\sqrt{g_{\varphi\varphi}}}{\sqrt{-g_{tt}}}\,\Omega, \quad v^2 := v_r^2 + v_\varphi^2. \tag{25}$$

When inflow or outflow is accompanied by fluid rotation ($\Omega \neq 0$), as we shall see below, v_r is not a convenient kinematic variable. Rather, we introduce the radial three-velocity in the corotating frame V_r, simply denoted by V. Since the corotating frame has the four-velocity vector $U^\alpha_{\rm corot} = (1,\ 0,\ 0\,,v_\varphi)/\sqrt{-g_{tt}(1-v_\varphi^2)}$, it is straightforward to show that V is related to v_r by

$$V = \frac{v_r}{\sqrt{1-v_\varphi^2}}. \tag{26}$$

Next, we intend to express the right-hand side of (23) in terms of $(r,\ V)$ and the constants of motion. From $u^\alpha u_\alpha = -1$, we obtain

$$u_t = -\frac{\sqrt{-g_{tt}}}{\sqrt{1-v^2}}. \tag{27}$$

Now, solving (24) for u_φ and using (27), we obtain

$$u_\varphi = \frac{4\pi\eta^2\mathcal{L}\sqrt{1-v^2} - \Omega_F\sqrt{-g_{tt}}\,g_{\varphi\varphi}n}{(4\pi\eta^2 h + g_{tt}n)\sqrt{1-v^2}}. \tag{28}$$

All we need now is to express v^2 in terms of V^2 to express $(u_t,\ u_\varphi)$ in terms of $(r,\ V)$. Before doing that, there is an interesting conclusion to draw, as follows: From the relation

$$v_r = \frac{C\sqrt{1-v^2}}{\sqrt{-g_{tt}}g_{\varphi\varphi}\,n} = \frac{C\sqrt{1-v_r^2-v_\varphi^2}}{\sqrt{-g_{tt}}g_{\varphi\varphi}\,n}, \tag{29}$$

we obtain

$$v_r^2 = \frac{C^2(1-v_\varphi^2)}{C^2 - g_{tt}g_{\varphi\varphi}^2 n^2}, \tag{30}$$

which upon using (26) yields the following:

$$V^2 = \frac{C^2}{C^2 - g_{tt}g_{\varphi\varphi}^2 n^2} < 1. \tag{31}$$

This may seem to show that the relative three-velocity of the fluid with respect to the corotating frame does not depend explicitly on the presence of any magnetic field, which is only apparently true. As we shall see below, n depends explicitly on $F^2 = F_{\mu\nu}F^{\mu\nu}$. It is obvious from (31) that $V^2 \to 1$ as $g_{tt} \to 0$, which is the case if $g_{tt}(r = r_h) = 0$, where r_h is the horizon of the BH.

In order to express v^2 in terms of V^2, we write v^2 as

$$\begin{aligned} v^2 &= v_r^2 + v_\varphi^2 = V^2(1-v_\varphi^2) + v_\varphi^2 \\ &= V^2\left(1 - \frac{(1-v^2)u_\varphi^2}{g_{\varphi\varphi}}\right) + \frac{(1-v^2)u_\varphi^2}{g_{\varphi\varphi}}, \end{aligned} \tag{32}$$

where u_φ is given in (28). Once u_φ is substituted into (32), we set $x = \sqrt{1-v^2}$, which occurs in the right-hand side of (28), and solve for x and then for v^2 in terms of V^2. We obtain two roots for the equation related by $v_1^2(\mathcal{L}) = v_2^2(-\mathcal{L})$. Since $\mathcal{L}$ can be given any sign, we will work with the solution v_1^2 by (A.1) given in the Appendix.

Since the right-hand side of (23) contains n, this can also be expressed as a function $(r,\ V)$ upon reversing (31), yielding

$$n(r,\ V) = \frac{C\sqrt{1-V^2}}{\sqrt{-g_{tt}}\,g_{\varphi\varphi}V}. \tag{33}$$

Given an equation of state expressing h in terms of n, we can also express enthalpy h as a function of the variables $(r,\ V)$. Finally, Eq. (23) takes the form

$$\begin{aligned} \mathcal{E}(r,\ V) = &-\left(h(r,\ V) + \frac{\Omega_F^2 g_{\varphi\varphi}(r)\,n(r,\ V)}{4\pi\eta^2}\right)u_t(r,\ V) \\ &+ \frac{\Omega_F g_{tt}(r)\,n(r,\ V)}{4\pi\eta^2}u_\varphi(r,\ V), \end{aligned} \tag{34}$$

where u_t and u_φ are given by (27) and (28), respectively, and v^2 is given in terms of V^2 in the Appendix by (A.1) and (A.2). Since $\mathcal{E}(r,\ V)$ is a global constant, it is the *Hamiltonian* of our system.

In the same manner, we can express the components of the magnetic field b^μ in the fluid frame in terms of $(r,\ V)$ as

$$\begin{aligned} b^t(r,\ V) &= -\frac{[1 + u^t(u_t - u_\varphi\Omega_F)]n}{\eta}, \\ b^r(r,\ V) &= -\frac{u^r(u_t + u_\varphi\Omega_F)n}{\eta} = -\frac{C(u_t + u_\varphi\Omega_F)}{\eta\sqrt{-g}}, \\ b^\varphi(r,\ V) &= -\frac{[\Omega_F(1 + u^\varphi u_\varphi) + u_t(u^\varphi + 2u^t\Omega_F)]n}{\eta}. \end{aligned} \tag{35}$$

Using all expressions given in (35), we express n explicitly depending on $F^2 = F_{\mu\nu}F^{\mu\nu}$ as

$$n^2 = \frac{\eta^2}{2}\,\frac{F^2}{g_{tt} + g_{\varphi\varphi}\Omega_F^2 + \left(u_t - u_\varphi\Omega_F\right)^2}. \tag{36}$$

3.2 Wind equation

The wind equation is obtained upon differentiating (34):

$$\mathrm{d}\mathcal{E}(r,\ V) = \mathcal{E}_{,r}\,\mathrm{d}r + \mathcal{E}_{,V}\,\mathrm{d}V = 0, \tag{37}$$

since $\mathcal{E}$ is a global constant of motion. Thus,

$$\frac{\mathrm{d}V}{\mathrm{d}r} = -\frac{\mathcal{E}_{,r}}{\mathcal{E}_{,V}}. \tag{38}$$

At the CPs where $(r,\ V) = (r_c,\ V_c)$, we have

$$\mathcal{E}_{,r}(r_c, V_c) = 0, \quad \text{and} \quad \mathcal{E}_{,V}(r_c, V_c) = 0. \tag{39}$$

Using the equation, $\mathrm{d}\ln h = a^2 \mathrm{d}\ln n$, for the adiabatic sound speed, we obtain

$$\left[\frac{\Omega_F n}{4\pi\eta^2 h u_t}(g_{tt}u_\varphi - \Omega_F g_{\varphi\varphi}u_t) - a^2\right](\ln n)_{,r} = (\ln u_t)_{,r} + \frac{\Omega_F n}{4\pi\eta^2 h u_t}(\Omega_F g_{\varphi\varphi}u_t - g_{tt}u_\varphi)_{,r}\,, \tag{40}$$

$$\left[\frac{\Omega_F n}{4\pi\eta^2 h u_t}(g_{tt}u_\varphi - \Omega_F g_{\varphi\varphi}u_t) - a^2\right](\ln n)_{,V} = (\ln u_t)_{,V} + \frac{\Omega_F n}{4\pi\eta^2 h u_t}(\Omega_F g_{\varphi\varphi}u_t - g_{tt}u_\varphi)_{,V}\,, \tag{41}$$

where $(.)_{,r}$ and $(.)_{,V}$ denote partial derivatives. In this Hamiltonian formalism, r and V are treated as independent variables. For instance, we have $(\Omega_F g_{\varphi\varphi}u_t - g_{tt}u_\varphi)_{,V} = \Omega_F g_{\varphi\varphi}u_{t,V} - g_{tt}u_{\varphi,V}$ and a similar expression for $(\Omega_F g_{\varphi\varphi}u_t - g_{tt}u_\varphi)_{,r}$, where $u_{t,V}$, $u_{\varphi,V}$, $u_{t,r}$, and $u_{\varphi,r}$ are evaluated using (27) and (28). Further, $(\ln n)_{,r}$, $(\ln n)_{,V}$, $(\ln u_t)_{,r}$, and $(\ln u_t)_{,V}$ are given by

$$(\ln n)_{,r} = -\frac{1}{2}\frac{g_{tt,r}}{g_{tt}} - \frac{g_{\varphi\varphi,r}}{g_{\varphi\varphi}}, \quad (\ln n)_{,V} = -\frac{1}{V(1-V^2)}\,, \tag{42}$$

$$(\ln u_t)_{,r} = \frac{1}{2}\frac{g_{tt,r}}{g_{tt}} + \frac{v}{1-v^2}v_{,r}, \quad (\ln u_t)_{,V} = \frac{v}{1-v^2}v_{,V}\,, \tag{43}$$

where $v_{,r}$ and $v_{,V}$ are evaluated using the expression of $v(r, V)$ given in the Appendix by (A.1) and (A.2). Equation (41) reduces to

$$a^2 = \frac{vV(1-V^2)}{1-v^2}v_{,V} + \frac{\Omega_F n}{4\pi\eta^2 h u_t}\big[(g_{tt}u_\varphi - \Omega_F g_{\varphi\varphi}u_t) - V(1-V^2)(g_{tt}u_\varphi - \Omega_F g_{\varphi\varphi}u_t)_{,V}\big]. \tag{44}$$

This is the most general equation for a^2 in the case of an axisymmetric MHD accretion onto a spherical BH. It is an implicit equation for the speed of sound, as its right-hand side also includes a^2 via $u_{t,V}$ and $u_{\varphi,V}$. This equation determines the speed of sound at the CP, and Eq. (40) determines the location of the CP once an equation of state (EoS) is supplied.

We see clearly from (44) that at the CP, $v^2 \neq a^2 \neq V^2$ in general. Even in the special case $\Omega_F = 0$ and/or $\eta = \infty$ (no magnetic field if $\Omega_F = 0$ and $\eta = \infty$),

$$a^2 = \frac{vV(1-V^2)}{1-v^2}v_{,V}, \quad (\Omega_F = 0 \text{ and/or } \eta = \infty), \tag{45}$$

is still different from V^2 and v^2, as can be checked from the expression of $v(r, V)$ in these special cases [which can be obtained from the general expressions (A.1) and (A.2)]:

$$v(r, V)^2 = \frac{16\pi^2(1-V^2)\mathcal{L}^2\eta^4 + V^2 g_{\varphi\varphi}(4\pi\eta^2 h + g_{tt}n)^2}{16\pi^2(1-V^2)\mathcal{L}^2\eta^4 + g_{\varphi\varphi}(4\pi\eta^2 h + g_{tt}n)^2}, \quad (\Omega_F = 0), \tag{46}$$

$$v(r, V)^2 = \frac{(1-V^2)\mathcal{L}^2 + V^2 g_{\varphi\varphi}h^2}{(1-V^2)\mathcal{L}^2 + g_{\varphi\varphi}h^2}, \quad (\eta = \infty), \tag{47}$$

where (n, h) are functions of (r, V) given by (33) and (60) [see also (34)]. However, if the angular momentum $\mathcal{L} = 0$, these last equations reduce to $v^2 = V^2$, and (45) yields $a^2 = V^2 = v^2$.

Another, much simpler, way to determine the CPs is to use the variables (r, n) instead of (r, V), as we did earlier in [15]. Using $u^\alpha u_\alpha = -1$, (13) and (24), we obtain

$$u_t(r, n) = -\frac{8\pi\mathcal{L}\eta^2\Omega_F^2 g_{tt}g_{\varphi\varphi}n^2 + [ng_{tt} + 4\pi\eta^2 h(n)]\sqrt{F(r, n)}}{2\Omega_F g_{\varphi\varphi}G(r, n)n}, \tag{48}$$

$$u_\varphi(r, n) = \frac{8\pi\mathcal{L}\eta^2[ng_{tt} + 4\pi\eta^2 h(n)] - \sqrt{F(r, n)}}{2G(r, n)}, \tag{49}$$

$$G(r, n) = g_{tt}^2 n^2 + 16\pi^2\eta^4 h(n)^2 + g_{tt}[\Omega_F^2 g_{\varphi\varphi}n + 8\pi\eta^2 h(n)]n, \tag{50}$$

$$F(r, n) = 64\pi^2\mathcal{L}^2\eta^4[ng_{tt} + 4\pi\eta^2 h(n)]^2 - 4[16\pi^2\mathcal{L}^2\eta^4 + \Omega_F^2(n^2 g_{tt}g_{\varphi\varphi}^2 - C^2)]G(r, n). \tag{51}$$

This transforms (23) to the following Hamiltonian expression.

$$\mathcal{E}(r, n) = -\left(h(n) + \frac{\Omega_F^2 g_{\varphi\varphi}(r)\,n}{4\pi\eta^2}\right)u_t(r, n) + \frac{\Omega_F g_{tt}(r)\,n}{4\pi\eta^2}u_\varphi(r, n). \tag{52}$$

Upon differentiating (52), we obtain

$$\mathrm{d}\mathcal{E}(r, n) = \mathcal{E}_{,r}\,\mathrm{d}r + \mathcal{E}_{,n}\,\mathrm{d}n = 0, \tag{53}$$

since $\mathcal{E}$ is a global constant of motion. Thus,

$$\frac{\mathrm{d}n}{\mathrm{d}r} = -\frac{\mathcal{E}_{,r}}{\mathcal{E}_{,n}}. \tag{54}$$

At the CPs where $(r, n) = (r_c, n_c)$ we have

$$\mathcal{E}_{,r}(r_c, n_c) = 0 \quad \text{and} \quad \mathcal{E}_{,n}(r_c, n_c) = 0. \tag{55}$$

The explicit forms of these two equations are derived from (40) and (41) upon making simple substitutions and noting that r and n are treated as independent variables:

$$0 = (\ln u_t)_{,r} + \frac{\Omega_F n}{4\pi\eta^2 h u_t}(\Omega_F g_{\varphi\varphi}u_t - g_{tt}u_\varphi)_{,r}, \tag{56}$$

$$a^2 = -n(\ln u_t)_{,n} + \frac{\Omega_F n}{4\pi\eta^2 h u_t} \times \left[(g_{tt}u_\varphi - \Omega_F g_{\varphi\varphi}u_t) - n(\Omega_F g_{\varphi\varphi}u_t - g_{tt}u_\varphi)_{,n}\right], \tag{57}$$

where the partial derivatives with respect to r and n are evaluated using (48) and (49). Equation (57) is another general implicit equation for a^2.

3.3 Polytropic fluid

If the equation of state is that of a polytropic fluid, then

$$p = Kn^{\gamma}, \quad \text{where } \gamma = (N+1)/N. \tag{58}$$

Here, K is a constant, m is the baryonic mass of the plasma particle, and N is the polytropic index. Following [15], we can show that the specific entropy satisfies

$$u^{\mu}\nabla_{\mu}s \propto u_{\mu}F^{\mu\nu}J_{\nu}. \tag{59}$$

Here, $J_{\nu} \propto u_{\nu}$ is the current density four-vector. In the case when the ideal MHD flow condition (6) holds, we have $u^{\mu}\nabla_{\mu}s = \partial_r s = 0$, implying an isentropic flow, and in this case the specific enthalpy and the three-dimensional sound speed are respectively given by [15,37]

$$h(r,V) = m\Big(1 + \frac{k\gamma n^{\gamma-1}(r,V)}{\gamma-1}\Big), \quad (K = mk) \tag{60}$$

$$a^2(r,V) = \frac{k\gamma(\gamma-1)n^{\gamma-1}}{(\gamma-1)+k\gamma n^{\gamma-1}}, \tag{61}$$

where $n(r,V)$ is given in (33). It is straightforward to show that

$$h = \frac{K\gamma n^{\gamma-1}}{a^2} = \frac{m(\gamma-1)}{(\gamma-1)-a^2}, \tag{62}$$

implying $a^2 < \gamma - 1$.

4 Special features in MHD Schwarzschild spherical accretion

4.1 Global parameter values

In this work, m is supposed to be proton mass $1.67262192 \times 10^{-27}$ kg ($m_g = 1.24187391 \times 10^{-54}$ in geometrized units). Unless otherwise stated, the other constants in geometrized units are as follows:

$$\begin{aligned}
&k = 5.08445 \times 10^{-17}, \quad C = \frac{7\times 10^{12} \times (M/M_{\odot})}{12\pi \times m(\text{kg}) \times c(\text{m/s})},\\
&N = \frac{4}{3}, \quad \gamma = \frac{7}{4},\\
&\mathcal{L} = 3.10m_g, \quad \Omega_F = 0, \quad \Phi_1 = -7\times 10^{-y},\\
&\eta = -\frac{C}{\Phi_1},
\end{aligned} \tag{63}$$

where M and $M_{\odot}$ are the masses of the BH and the sun, respectively, and c is the speed of light. The value of C corresponds to 0.001 times the Eddington rate, which is 1.44×10^{15} (kg/s), taking the average ratio r/H, where H is the height of the disk, to be 0.6. To show the main features of MHD flow, we mainly focus on the case $\Omega_F = 0$ unless otherwise stated. Note that if a flow solution passes thorough the Alfvén point in the (r, V)-plane or the (r, n)-plane, where the denominator of (28) becomes zero, the regularity condition (28) yields a constraint between Ω_F and $\mathcal{L}$ that does not allow the case $\Omega_F = 0$, $\mathcal{L} \neq 0$, as discussed in [30,36,38]. In this paper, we focus on solutions that do not cross the Alfvén point, which happens when η is large or the corresponding magnetic field is weak. Therefore, Ω_F and $\mathcal{L}$ are independent of each other. For the case of the Schwarzschild BH, the MHD accretion was intensively studied in [27] and other references therein. In this work we aim to show those special features of flows not yet investigated in the scientific literature.

4.2 Results

As an initial condition, we assume that the outer boundary of the flow (of the disk) is at $r_{\text{out}} = 100r_g$ with $r_g = GM/c^2$, and that $M = M_{\odot}$. We have also examined the case with $r_{\text{out}} = 1000r_g$, and the main features remain absolutely the same, with the only difference being that the lower possible initial speed V_{ℓ} of the in/outflow at r_{out} depends on r_{out} itself and on the other parameters. For $\Omega_F = 0$, the expression of u_{φ} (28) is positive if its denominator is positive. Thus, the lower speed V_{ℓ} at r_{out} is a solution to $4\pi\eta^2 h + g_{tt}n = 0$. For fixed r_{out}, the lower speed V_{ℓ} is an increasing function of the intensity of the magnetic field Φ_1 (63), as shown in Fig. 2. In this figure we plot $\mathcal{E}/m_g$ ($\mathcal{E}$ in the units of m_g) versus V upon fixing r at r_{out} and varying the intensity of the magnetic field Φ_1 (63). Left panel: $r_{\text{out}} = 100r_g$ and $y = 8$. Below the speed $V_{\ell} = 0.02581$ the in/outflow is not possible. Above $\mathcal{E}_{\ell} = 1.51627$, there is only one possible speed of the flow. Below $\mathcal{E}_{\ell}$ and above $\mathcal{E}_{\text{m}} = 0.24663$, there are two possible initial speeds of the flow (relativistic and non-relativistic). Intermediate panel: $r_{\text{out}} = 100r_g$ and $y = 7.5$. Upon increasing the intensity of the magnetic field Φ_1, $V_{\ell} = 0.339$ increases and the minimum of $\mathcal{E}_{\ell}$ disappears. There is no possible flow below $\mathcal{E}_{\ell} = 1.12535$, and above it only relativistic flow is possible. Right panel: $r_{\text{out}} = 1000r_g$ and higher magnetic field $y = 6.7$. In this case, $V_{\ell} = 0.15224$ (for the corresponding case $r_{\text{out}} = 100r_g$ and $y = 6.7$, $V_{\ell} = 0.99786$ is extremely relativistic). No possible flow occurs below $\mathcal{E}_{\ell} = 1.01760$. As Φ_1 increases, the magnetic pressure increases as well, preventing the flow from advancing unless its initial speed exceeds some lower limit V_{ℓ} at the outer boundary r_{out} of the disk.

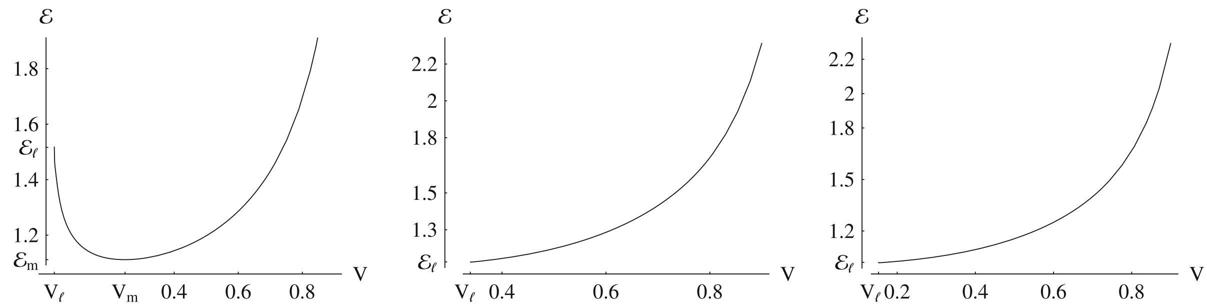

Fig. 2 $\mathcal{E}/m_g$ ($\mathcal{E}$ in the units of m_g) versus V upon fixing r at r_out and varying the intensity of the magnetic field Φ_1 (63). Left panel: $r_\mathrm{out} = 100r_g$ and $y = 8$. Below the speed $V_\ell = 0.02581$ the in/outflow is not possible. Above $\mathcal{E}_\ell = 1.51627$, there is only one possible speed of the flow. Below $\mathcal{E}_\ell$ and above $\mathcal{E}_\mathrm{m} = 1.11166$ (corresponding to $V_\mathrm{m} = 0.24663$), there are two possible initial speeds of the flow (relativistic and non-relativistic). Intermediate panel: $r_\mathrm{out} = 100r_g$ and $y = 7.5$. Upon increasing the the intensity of the magnetic field Φ_1, $V_\ell = 0.339$ increases and the minimum of $\mathcal{E}_\ell$ disappears. No possible flow occurs below $\mathcal{E}_\ell = 1.12535$ and above it only relativistic flow is possible. Right panel: $r_\mathrm{out} = 1000r_g$ and higher magnetic field $y = 6.7$. In this case $V_\ell = 0.15224$ (for the corresponding case $r_\mathrm{out} = 100r_g$ and $y = 6.7$, $V_\ell = 0.99786$ is extremely relativistic). No possible flow happens below $\mathcal{E}_\ell = 1.01760$

4.2.1 Outflow with constant limiting speed—inflow in the vicinity of the horizon

In Fig. 3, we plot V versus r/r_g for $\mathcal{E} = \mathcal{E}(100r_g, 0.05) = 1.28736$ and $y = 8$ with conditions at the outer boundary $r_\mathrm{out} = 100r_g$ and $V_\mathrm{out} = 0.05$. The left panel depicts the outflow. If the fluid is ejected at $r = 43.1659r_g$ with a speed of $V_i = 0.371$, it may flow along the upper branch, reaching the final speed $V_f = 0.629765$ at spatial infinity, as can be seen from the Taylor expansion

$$\begin{aligned}\mathcal{E}(r, V) &= 1.28736 - \frac{1900.95}{r} \\ &\quad +\Big(1.34362 - \frac{1984.02}{r}\Big)(V - 0.629765) \\ &\quad +\Big(3.17027 - \frac{4681.3}{r}\Big)(V - 0.629765)^2 + \cdots\end{aligned} \tag{64}$$

The fluid may flow along the lower path, reaching a zero speed at spatial infinity; more precisely, the speed at $r = 10^{100+q}$ and $q > 0$ is $V = 5.22082 \times 10^{-198-2q}$. The right panel depicts the inflow. In the vicinity of the horizon, the level curve $\mathcal{E} = \mathcal{E}(100r_g, 0.05) = 1.28736$ has another physical branch, where the fluid may flow along the upper branch and cross the horizon with a speed $V = 1$, or flow along the lower branch and cross the horizon with a speed $V = 0.0387543$. In this region the magnetic field is so strong that the fluid has to start its journey with a speed nearing 0.85, with r being around $2 + 7 \times 10^{-9}$.

4.2.2 Non-critical global flow

Keeping the same conditions at the outer boundary, $r_\mathrm{out} = 100r_g$ and $y = 8$, and increasing $\mathcal{E}$ to $\mathcal{E} = 10.0874$, the flow becomes global and non-critical, as shown in Fig. 4. In each of the four panels, the plot passes near the CP [defined by $\mathcal{E}_{,r}(r_c, V_c) = 0$ and $\mathcal{E}_{,V}(r_c, V_c) = 0$] or by $\mathcal{E}_{,r}(r_c, n_c) = 0$ and $\mathcal{E}_{,n}(r_c, n_c) = 0$), but not through it. Based on the left panel of Fig. 2, the level curve of $\mathcal{E} = 10.08736$ in the rV-plane mathematically has two branches; physically speaking, only the upper branch (relativistic branch) is relevant. This is because, for the lower non-relativistic branch, the equation $\mathcal{E} = 10.08736 = \mathcal{E}(100r_g, V)$ has a solution $V = 0.00051953 < V_\ell = 0.02581$: The magnetic pressure at the outer boundary $100r_g$ is such that flow with speed below V_ℓ is allowed. We see that the radial component of the magnetic field, b^r, jumps high from its outer value $b^r{}_\mathrm{out} = 11.8193$ G to about 3300 G, then drops to about half that value at the horizon $r_\mathrm{h} = 2r_g$. As to the radial three-speed V, it decreases from $V_\mathrm{out} = 0.995119$ to $V(r = r_c) = 0.880467 > V_c = 0.841218$, then increases to its final value $V(r = r_\mathrm{h}) = 1^-$. This global accretion flow starting at $r_\mathrm{out} = 100r_g$ with such high speed is possible if, for instance, the fluid was ejected (an outflow) by a companion star.

4.2.3 Critical global flow

A global critical flow is observed for $r_\mathrm{out} = 100r_g$ with $y = 8$ if we take $\mathcal{E} = 10.02082$, as shown in Fig. 5, where each plot passes through the corresponding CP. In this case as well, only the upper relativistic branch $V(r)$ is relevant. This case shows a special feature compared to the case of Fig. 4: each plot is continuous at the CP, but a corner appears there indicating a non-smoothness in the slope [exception: the slope of $F^2(r)$ appears to be continuous at the CP]. The non-smoothness in the slope is not an isolated case; rather, we observed such behavior for other, even non-critical, values of $\mathcal{E}$, as 10.02126.

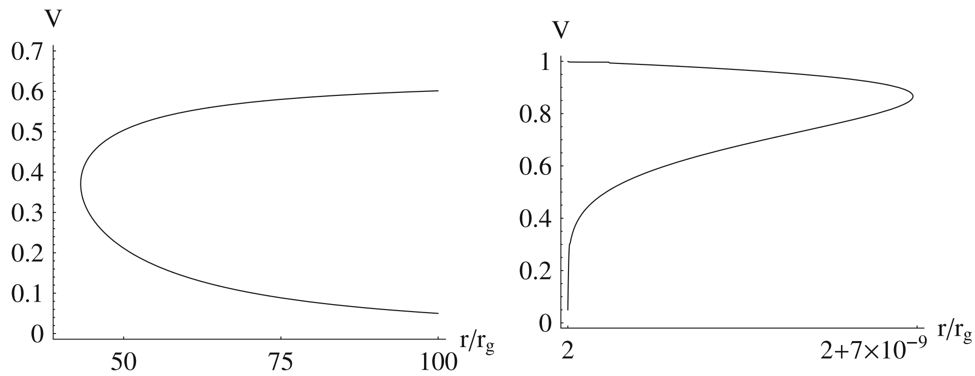

Fig. 3 V versus r/r_g for $\mathcal{E} = \mathcal{E}(100r_g, 0.05) = 1.28736$ ($\mathcal{E}/m_g = 1.28736$) and $y = 8$. Left panel: outflow with constant limiting speed. If the fluid is ejected at $r = 43.1659r_g$ with a speed of $V_i = 0.371$, it may flow along the upper branch, reaching the final speed $V_f = 0.629765$ at spatial infinity (note that the speed of the fluid as it reaches $100r_g$ is 0.629765, as can also be seen from the left panel of Fig. 2). The fluid may flow along the lower path, reaching another nearly zero speed at spatial infinity (note that the speed of the fluid as it reaches $100r_g$ is 0.05, as can also be seen from the left panel of Fig. 2). Right panel: inflow. In the vicinity of the horizon, the level curve $\mathcal{E} = \mathcal{E}(100r_g, 0.05) = 1.28736$ has another branch, where the fluid may flow along the upper branch and cross the horizon with a speed $V = 1$, or flow along the lower branch and cross the horizon with a speed $V = 0.0387543$. In this region the magnetic field is so strong that the fluid has to start its journey with a speed nearing 0.85, with r being around $2 + 7 \times 10^{-9}$

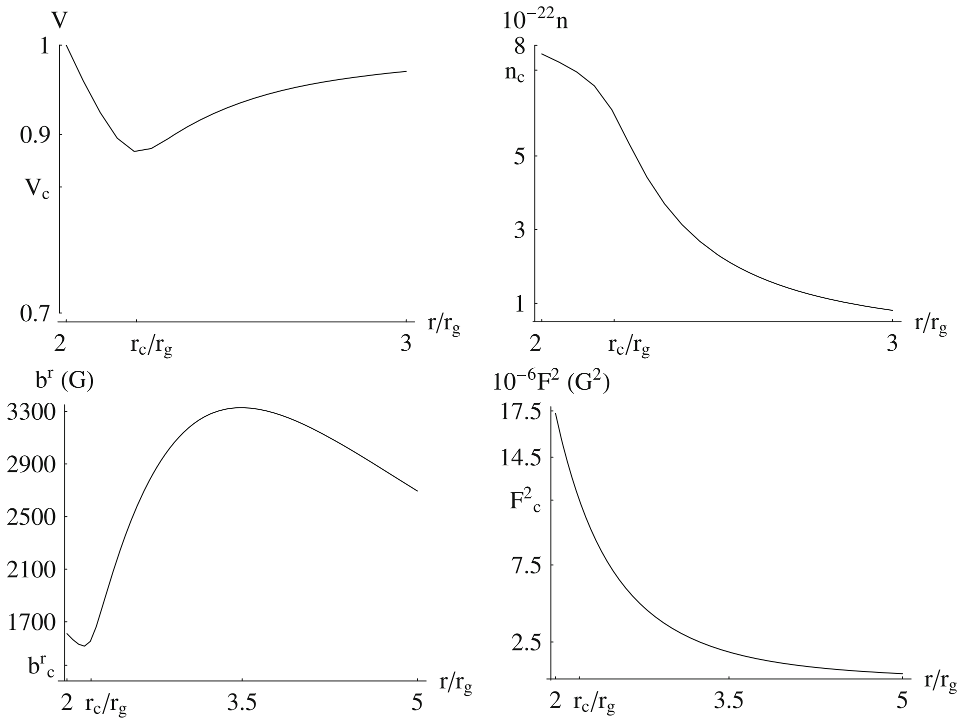

Fig. 4 Non-critical global flow. Plots of V, n, b^r, and F^2 versus r/r_g for $\mathcal{E} = 10.08736$ and $y = 8$ with the outer boundary $r_{\text{out}} = 100r_g$. In each panel the plot passes near the CP [defined by $\mathcal{E}_{,r}(r_c, V_c) = 0$ and $\mathcal{E}_{,V}(r_c, V_c) = 0$], but not through it. At the CP we have $r_c = 3258.28 = 2.20657r_g$, $V_c = 0.841218$, $n_c = 7.32727 \times 10^{22}$, ${b^r}_c = 1369.31$ G, ${F^2}_c = 1.1711 \times 10^7$ G^2. At the outer boundary of the disk we have $r_{\text{out}} = 100r_g$, $V_{\text{out}} = 0.995119$, $n_{\text{out}} = 1.70121 \times 10^{18}$, ${b^r}_{\text{out}} = 11.8193$ G, ${F^2}_{\text{out}} = 2.77628$ G^2. Here, n_c, ${b^r}_c$, and ${F^2}_c$ are the values of $n(r, V)$, $b^r(r, V)$, and $F^2(r, V)$ at the point $(r, V) = (r_c, V_c)$

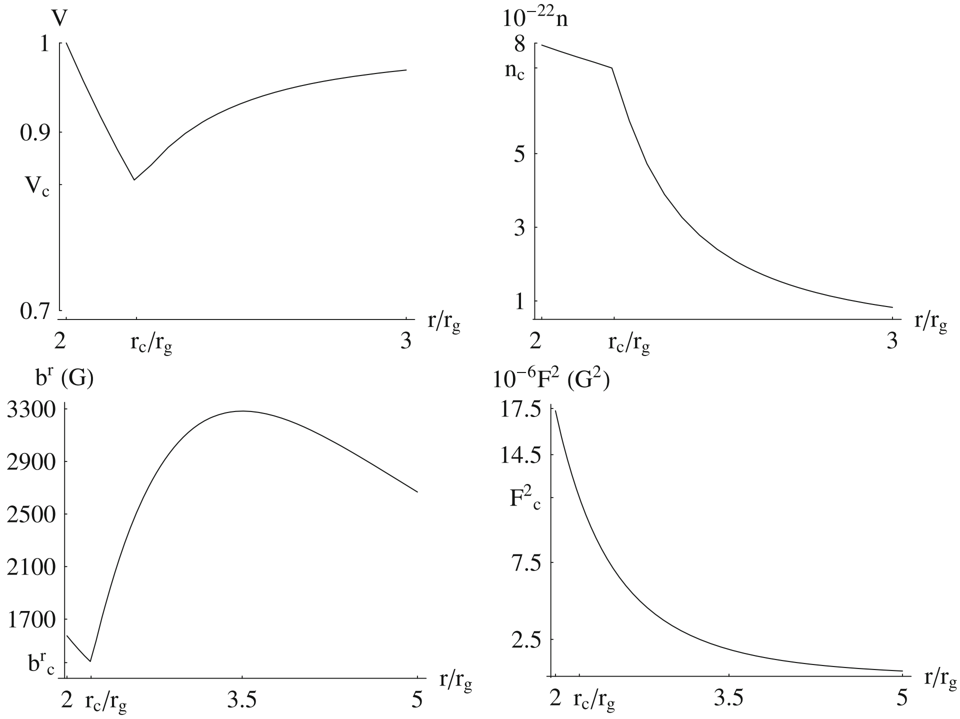

Fig. 5 Critical global flow. Plots of V, n, b^r, and F^2 versus r/r_g for $\mathcal{E} = 10.02082$ and $y = 8$ with the outer boundary $r_{\text{out}} = 100r_g$. In each panel the plot passes through the corresponding CP. At the CP we have $r_c = 3258.28 = 2.20657r_g$, $V_c = 0.841218$, $n_c = 7.32727 \times 10^{22}$, ${b^r}_c = 1369.31$ G, ${F^2}_c = 1.1711 \times 10^7$ G^2. At the outer boundary of the disk we have $r_{\text{out}} = 100r_g$, $V_{\text{out}} = 0.995053$, $n_{\text{out}} = 1.71276 \times 10^{18}$, ${b^r}_{\text{out}} = 11.7404$ G, ${F^2}_{\text{out}} = 2.77628$ G^2

4.2.4 Magnetically arrested-disk state

In order to observe new phenomena, we decrease the intensity of the magnetic field, taking $y = 11$ and keeping $r_{\text{out}} = 100r_g$. All fluid motions met in the case $y = 8$ are also met in this case $y = 11$ and plus. For this case, a similar curve to the left panel of Fig. 2 exists, however, it extends up to infinity in both limits $V \to 0^+$ and $V \to 1^-$. This means that for any[2] $\mathcal{E} > \mathcal{E}_{\text{m}} = 1.11166$, there are always two branches in the rV-plane, non-relativistic and relativistic, for any initial speed V_{out} of the flow (in or out) at $r_{\text{out}} = 100r_g$. We consider the magnetically arrested-disk, non-critical, state $\mathcal{E} = \mathcal{E}(100r_g, 0.00052) = 10.08127$ corresponding to $V_{\text{out}} = 0.00052$, $n_{\text{out}} = 3.29906 \times 10^{22}$, ${b^r}_{\text{out}} = 0.00116635$ G, ${F^2}_{\text{out}} = 2.77632 \times 10^{-6}$ G^2 for the non-relativistic branch, and to $V_{\text{out}} = 0.995113$, $n_{\text{out}} = 1.70226 \times 10^{18}$, ${b^r}_{\text{out}} = 0.011812$ G, ${F^2}_{\text{out}} = 2.77628 \times 10^{-6}$ G^2 for the relativistic branch. The corresponding plots are depicted in Fig. 6. For the non-relativistic branch in the rV-plane, the fluid crosses the horizon at $r = r_{\text{h}}$ with a speed $V_{\text{h}} = 0.00249148$ and, because of the conservation law (33), n diverges at $r = r_{\text{h}}$ where $g_{tt}(r_{\text{h}}) = 0$. The sharp decrease of the speed in the non-relativistic branch $V(r)$, from about V_c to V_{h} within an interval of extent $\Delta r = 0.20657r_g$, accompanied by a similar decrease in b^r and a sharp increase in n, is a signal of the magnetically arrested-disk state in the corona Δr of high density ($n \to \infty$ as $r \to r_{\text{h}}$) around the horizon. We have obtained similar results for $y = 9.5$ for fixed $\mathcal{E}$, and the sharp decrease in $V(r)$ occurs at the same location.

4.2.5 Shock-induced flow

According to (59), if the ideal MHD flow condition (6) is violated, the isentropic condition is also violated, and vice versa. Our enthalpy formula (60) is valid under the assumption of isentropic flow. In order to observe a shock-induced flow at some location r_{sh}, we have to envisage a flow where the entropy is constant in the pre-shock flow s_{pre} and constant in the post-shock flow s_{post}, and has a finite *positive* jump between the two constants at r_{sh}:

$$\Delta s\big|_{r_{\text{sh}}} = s_{\text{post}} - s_{\text{pre}} > 0. \tag{65}$$

The value of r_{rh} depends on that of Δs. According to (59), a shock state generates a momentary electric current in the flow.

[2] The actual value of $\mathcal{E}_{\text{m}}$ for this case is slightly different from that given in the caption of Fig. 2. The values are $\mathcal{E}_{\text{m}} = 1.111661501620652$ for $y = 8$ and $\mathcal{E}_{\text{m}} = 1.1116615015528608$ for $y = 11$. The values of V_{m} are the same.

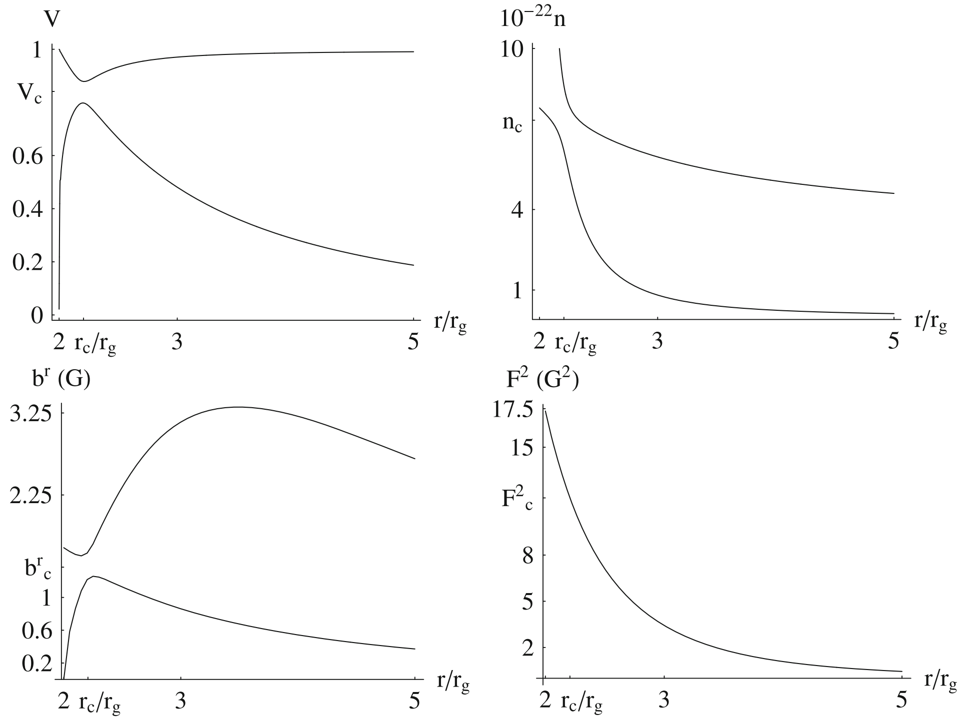

Fig. 6 Magnetically arrested-disk, non-critical, global flow. Plots of V, n, b^r, and F^2 versus r/r_g for $\mathcal{E} = \mathcal{E}(100r_g, 0.00052) = 10.08127$ and $y = 11$ with the outer boundary $r_{\text{out}} = 100r_g$. This case corresponds to $V_{\text{out}} = 0.00052$, $n_{\text{out}} = 3.29906 \times 10^{22}$, $b^r{}_{\text{out}} = 0.00116635$ G, $F^2{}_{\text{out}} = 2.77632 \times 10^{-6}$ G^2 for the non-relativistic branch, and to $V_{\text{out}} = 0.995113, n_{\text{out}} = 1.70226 \times 10^{18}, b^r{}_{\text{out}} = 0.011812$ G, $F^2{}_{\text{out}} = 2.77628 \times 10^{-6}$ G^2 for the relativistic branch. At the CP we have $r_c = 3258.28 = 2.20657r_g$, $V_c = 0.841217$, $n_c = 7.32733 \times 10^{22}$, $b^r{}_c = 1.36931$ G, $F^2{}_c = 11.711$ G^2. The upper branch in the rn-plane is the non-relativistic one and the lower branch is the relativistic one. The two branches in the rb^r-plane are in one-to-one correspondence with the branches in rV-plane. The two branches in the rF^2-plane coincide

We refine some of the parameters in (63), reducing the values of $(k,\ \mathcal{L})$, taking $y = 8$, and keeping the other parameters unchanged.

$$\begin{aligned} &k = 5.08445 \times 10^{-19}, \quad \mathcal{L} = 1.90m_g, \\ &\Phi_1 = -7 \times 10^{-y}, \quad y = 8. \end{aligned} \tag{66}$$

In shock-induced flow, one usually keeps both $\mathcal{L}$ and $\mathcal{E}$ constant and considers changes in the entropy, number (or rest-mass) density, the three-speed, and all that depends on n and V as the magnetic field components [26,36,39]. Shock-induced flows with energy drops are also possible. In fact, these are the most realistic shock-induced flows. We have obtained instances of such flows, taking $\mathcal{L}$ as in (66) and allowing $\mathcal{E}$ to drop by some amount. However, in this work we will consider only flows with no loss of energy. In the following, we hold $\mathcal{L}$ constant as in (66) and we keep $\mathcal{E} = 0.99468564m_g$, the values used in Fig. 7 depicting a non-violent shock. The pre-shock plots are in red and the post-shock plots are in black. Since for polytropic fluids, k is related to the entropy, we had to vary its value from red ($k_{\text{pre}} = 5.08445 \times 10^{-19}$) to black ($k_{\text{post}} = 1.7k_{\text{pre}}$) plots. From pre-shock state to post-shock state, we see a net decrease in the three-speed and a net increase in the number density at the shock location $r_{\text{sh}} = 52.9676r_g$, which is determined numerically upon imposing a discontinuity constraint, Eq. (10) of [26] (see also [36]). In Fig. 7 the values of $V_{\text{pre}} = 0.14353$ and $n_{\text{pre}} = 4.25481 \times 10^{20}$ correspond to points on the red plots (pre-shock state); their values at the post-shock state are $V_{\text{post}} = 0.117889$ and $n_{\text{post}} = 5.19795 \times 10^{20}$. The fluid crosses the horizon at $r \to r_{\text{h}} = 2r_g$ with $n = 5.20664 \times 10^{22}$ and $V \to 1$.

The jump in the value of the entropy is evaluated upon integrating the thermodynamic relation $T ds = dh - (dp/n)$ along the dashed vertical line $r = r_{\text{sh}}$ from the pre-shock point (on the red plot) to the post-shock point (on the black plot) and assuming $T = (mk/k_{\text{B}})n^{\gamma-1}$ for a perfect gas (k_{B} being the Boltzmann constant). We obtain

$$\Delta s = \frac{k_{\text{B}}}{\gamma - 1} \ln\left(\frac{k_{\text{post}}}{k_{\text{pre}}}\right) = \frac{4k_{\text{B}}}{3} \ln(1.7) > 0, \tag{67}$$

which does not depend on r_{sh} and depends only on $k_{\text{post}}/k_{\text{pre}}$ and γ. We have noted that the shock state disappears if we choose $k_{\text{post}} = 2k_{\text{pre}}$, and this may be a sign that the jump in the entropy could have an upper limit beyond which no shock occurs. This upper limit is certainly not universal, as it is parameter dependent.

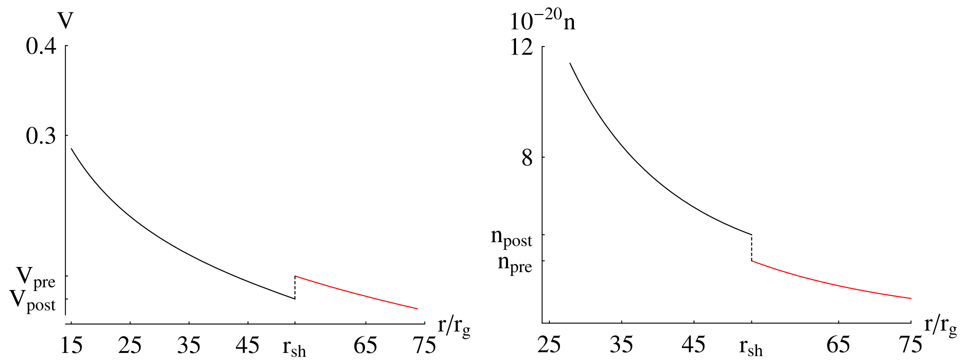

Fig. 7 Shock-induced global flow. Plots of V and n versus r/r_g for $\mathcal{E} = 0.99468564m_g$, $\mathcal{L} = 1.90m_g$, and $y = 8$, with the other parameters remaining unchanged. The pre-shock plots are in red ($k_{\text{pre}} = 5.08445 \times 10^{-19}$) and the post-shock plots are in black ($k_{\text{post}} = 1.7k_{\text{pre}}$). The shock occurs at $r_{\text{sh}} = 52.9676r_g$, with $V_{\text{pre}} = 0.14353$ and $n_{\text{pre}} = 4.25481 \times 10^{20}$ [corresponding to points on the red plots (pre-shock state)], and $V_{\text{post}} = 0.117889$ and $n_{\text{post}} = 5.19795 \times 10^{20}$ [corresponding to points on the black plots (post-shock state)]. In the limit $r \to r_{\text{h}} = 2r_g$, $n \to 5.20664 \times 10^{22}$ and $V \to 1$

Table 1 Quantum effects on the shock location. Here, $\Delta r_{\text{sh}} = r_{\text{sh-Q}} - r_{\text{sh}}$, $r_{\text{sh-Q}}$ is the quantum-corrected value of the shock location, and $r_{\text{sh}} = 52.9676r_g$ is the (classical) value previously determined in Fig. 7

α	0.5	3	5
$\Delta r_{\text{sh}}/r_g$	0.492335×10^{-10}	2.80259×10^{-10}	4.65832×10^{-10}

It was shown in [39] that the shock location r_{sh} depends on the intensity of the magnetic field $|\Phi_1|$, that it increases with increasing $|\Phi_1|$, and that the shock disappears above some limiting value Φ_{lim}. That is, higher values of the magnetic field push the shock location outward, not favoring shock states. We confirm this finding, as the discontinuity constraint, Eq. (10) of [26], cannot be satisfied above some value of $|\Phi_1|$. For instance, we have obtained $r_{\text{sh}} = 8.37699r_g$, $52.9676r_g$, $69.2255r_g$ for $|\Phi_1| = 7 \times 10^{-8.5} = 2.21359 \times 10^{-8}$, 7×10^{-8}, 8×10^{-8}, respectively. We have obtained the further result that the discontinuity constraint cannot be satisfied above some value of $k_{\text{post}}/k_{\text{pre}}$, and thus no shock state. As emphasized in [39], these shock states are not isolated, that is, we have obtained many of them for sets of the parameters different from those in (66). However, our main purpose in this work is not to give a detailed discussion of the shock state; rather, it is to show how to apply the Hamiltonian approach, skipping thus the task of integrating differential equations, as done so far in the scientific literature, and to determine the profile of the MHD accretion, particularly, the existence of the shock state. In the remaining section, we will consider the quantum corrected Schwarzschild BH and investigate the shock states of MHD accretion onto this BH.

5 MHD Accretion for the quantum corrected Schwarzschild BH

Here, we consider the quantum corrected Schwarzschild BH [40,41]

$$ds^2_{\text{MS}} = -f(r)\mathrm{d}t^2 + f(r)^{-1}\mathrm{d}r^2 + r^2\mathrm{d}\Omega^2, \tag{68}$$

where

$$f(r) = 1 - \frac{2M}{r} + \frac{\alpha M^2}{r^4}. \tag{69}$$

Here, the parameter α is defined as $\alpha = 16\sqrt{3}\pi\gamma_{\text{Imm}}{}^3\ell_p^2$ with $\ell_p = \sqrt{G\hbar}$ denotes the Planck length and γ_{Imm} is the Immirzi parameter. It is worth noting that the form (68) of the metric is valid for

$$r \geq r_{\text{b}} = \left(\frac{\alpha GM}{2}\right)^{\frac{1}{3}}. \tag{70}$$

For illustration we take $\alpha = 0.5,\ 3,\ 5$. Within the values of the parameters used in Fig. 7 and in (66), we are guaranteed that $r_{\text{b}} < r_{\text{h}} = 2r_g$.

Table 1 depicts the variation of Δr_{sh} in terms of α , where $\Delta r_{\text{sh}} = r_{\text{sh-Q}} - r_{\text{sh}}$, $r_{\text{sh-Q}}$ is the quantum-corrected value of the shock location, and $r_{\text{sh}} = 52.9676 r_g$ is the (classical) value previously determined in Fig. 7. We see that Δr_{sh} slightly increases with α, which implies that quantum effects do not favor shock states by pushing the shock location outward.

6 Conclusion

In this article, we have formulated the accretion dynamics of an MHD fluid onto a spherical BH using a Hamiltonian framework. Under the assumptions of ideal MHD, and utilizing a few conservation laws of energy-angular momentum and particle number, we are able to determine a Hamiltonian expression which is used to derive the Hamilton equations and then their solutions. It is presumed that the flow occurred in the equatorial plane and that the only non-vanishing component of a magnetic field is the azimuthal one. In the background of a Schwarzschild BH, we have found the inflow/outflow conditions depending on the three-velocity and the energy parameters. The phenomena of relativistic and non-relativistic flows as well as no-flow are also observed. We have also examined the critical flows (i.e., the flows whose phase trajectories pass through the critical point) as well as non-critical flows (i.e., the flows where phase trajectories pass near the critical point but not through the CP) for the Schwarzschild BH. In the latter scenario, we have also observed a global flow, i.e., fluid flow starting from the outer edge of the disk and ending at the event horizon. We have also noted that shocks in MHD plasma near the BH cause particle number density in the MHD flow to increase but three-velocity to decrease locally near the shock region.

In future investigations, we would like to develop the Hamiltonian formulation of MHD flow near a Kerr BH and explore various kinds of flows along with different equations of state. In addition, we are interested in the question of how shocks in MHD plasma near a BH can generate highly magnetized plasma, and whether various quantum corrections to BH geometry can have deeper or observable effects in the accretion process.

Acknowledgements MJ would like to thank Zhejiang University of Technology, Hangzhou, China for providing hospitality where part of this work was completed. We would also thank Yen Chin Ong for useful discussions on this project.

Data Availability Statement This manuscript has no associated data. [Author's comment: Data sharing not applicable to this article as no datasets were generated or analysed during the current study.]

Code Availability Statement Code/software will be made available on reasonable request. [Author's comment: The code/software generated during and/or analysed during the current study is available from the corresponding author on reasonable request.]

Funded by SCOAP[3].

Appendix: Roots of (32)

Substituting u_φ given in (28) into (32) and setting $x = \sqrt{1-v^2}$, we obtain two roots for v^2 related by $v_1^2(\mathcal{L}) = v_2^2(-\mathcal{L})$. Since $\mathcal{L}$ can be given any sign, we will work with the solution v_1^2. The two solutions are given by

$$v^2 = v_1^2 = 1 - \left(\frac{4\pi \mathcal{L} \eta^2 \Omega_F \sqrt{-g_{tt}}\, g_{\varphi\varphi} n \left(1 - V^2\right) - \sqrt{H_1}}{H_2} \right)^2, \textit{and} \tag{A.1}$$

$$v^2 = v_2^2 = 1 - \left(\frac{4\pi \mathcal{L} \eta^2 \Omega_F \sqrt{-g_{tt}}\, g_{\varphi\varphi} n \left(1 - V^2\right) + \sqrt{H_1}}{H_2} \right)^2, \tag{A.2}$$

where

$$\begin{aligned} H_1 = &\left(1 - V^2\right) g_{\varphi\varphi} \left(4\pi\eta^2 h + g_{tt} n\right)^2 \\ &\times \left[16\pi^2 \left(1 - V^2\right) \mathcal{L}^2 \eta^4 + \Omega_F^2 g_{tt} g_{\varphi\varphi}^2 n^2 \right. \\ &\left. + g_{\varphi\varphi} \left(4\pi\eta^2 h + g_{tt} n\right)^2 \right], \end{aligned} \tag{A.3}$$

$$H_2 = 16\pi^2 \left(1 - V^2\right) \mathcal{L}^2 \eta^4 + g_{\varphi\varphi} \left(4\pi\eta^2 h + g_{tt} n\right)^2. \tag{A.4}$$

References

1. J.R. Oppenheimer, H. Snyder, On continued gravitational contraction. Phys. Rev. Ser. **56**, 455 (1939). https://doi.org/10.1103/PhysRev.56.455
2. B.L. Webster, P. Murdin, Cygnus X-1-a spectroscopic binary with a heavy companion? Nature (London) **235**, 37 (1972). https://doi.org/10.1038/235037a0
3. C.T. Bolton, Identification of Cygnus X-1 with HDE 226868. Nat. Ser. **235**, 271 (1972). https://doi.org/10.1038/235271b0
4. J.E. McClintock, R.A. Remillard, The black hole binary A0620-00. Astrophys. J Ser. **308**, 110 (1986). https://doi.org/10.1086/164482
5. M. Schmidt, 3C 273: a star-like object with large red-shift. Nat. Ser. **197**, 1040 (1963). https://doi.org/10.1038/1971040a0
6. LIGO Scientific, Virgo Collaboration, B.P. Abbott et al., Observation of gravitational waves from a binary black hole merger. Phys. Rev. Lett. **116**, 061102 (2016). https://doi.org/10.1103/PhysRevLett.116.061102. arXiv:1602.03837

7. Event Horizon Telescope Collaboration, K. Akiyama et al., First M87 Event Horizon Telescope results. IV. Imaging the central supermassive black hole. Astrophys. J. Lett. **875**, L4 (2019). https://doi.org/10.3847/2041-8213/ab0e85. arXiv:1906.11241
8. Event Horizon Telescope Collaboration, K. Akiyama et al., First Sagittarius A* Event Horizon Telescope results. I. The shadow of the supermassive black hole in the Center of the Milky Way. Astrophys. J. Lett. **930**, L12 (2022). https://doi.org/10.3847/2041-8213/ac6674. arXiv:2311.08680
9. H. Bondi, On spherically symmetrical accretion. Mon. Not. R. Astron. Soc. Ser. **112**, 195 (1952). https://doi.org/10.1093/mnras/112.2.195
10. F.C. Michel, Accretion of matter by condensed objects. Astrophys. Space Sci. Ser. **15**, 153 (1972). https://doi.org/10.1007/BF00649949
11. S. Nampalliwar, S. Kumar, K. Jusufi, Q. Wu, M. Jamil, P. Salucci, Modeling the Sgr A* black hole immersed in a dark matter spike. Astrophys. J. Ser. **916**, 116 (2021). https://doi.org/10.3847/1538-4357/ac05cc. arXiv:2103.12439
12. S. Bahamonde, M. Jamil, Accretion processes for general spherically symmetric compact objects. Eur. Phys. J. C Ser. **75**, 508 (2015). https://doi.org/10.1140/epjc/s10052-015-3734-9. arXiv:1508.07944
13. M. Jamil, M.A. Rashid, A. Qadir, Charged black holes in phantom cosmology. Eur. Phys. J. C Ser. **58**, 325 (2008). https://doi.org/10.1140/epjc/s10052-008-0761-9. arXiv:0808.1152
14. M.A. Abramowicz, P.C. Fragile, Foundations of black hole accretion disk theory. Living Rev. Relativ. **16**, 1 (2013). https://doi.org/10.12942/lrr-2013-1. arXiv:1104.5499
15. A.K. Ahmed, M. Azreg-Aïnou, M. Faizal, M. Jamil, Cyclic and heteroclinic flows near general static spherically symmetric black holes. Eur. Phys. J. C Ser. **76**, 280 (2016). https://doi.org/10.1140/epjc/s10052-016-4112-y. arXiv:1512.02065
16. R. Yang, Quantum gravity corrections to accretion onto a Schwarzschild black hole. Phys. Rev. D Ser. **92**, 084011 (2015). https://doi.org/10.1103/PhysRevD.92.084011. arXiv:1504.04223
17. M. Azreg-Aïnou, A.K. Ahmed, M. Jamil, Spherical accretion by normal and phantom Einstein–Maxwell-dilaton black holes. Class. Quantum Gravity Ser. **35**, 235001 (2018). https://doi.org/10.1088/1361-6382/aae997. arXiv:1809.03320
18. M.U. Farooq, A.K. Ahmed, R.-J. Yang, M. Jamil, Accretion on high derivative asymptotically safe black holes. Chin. Phys. C Ser. **44**, 065102 (2020). https://doi.org/10.1088/1674-1137/44/6/065102
19. S. Yang, C. Liu, T. Zhu, L. Zhao, Q. Wu, K. Yang et al., Spherical accretion flow onto general parameterized spherically symmetric black hole spacetimes. Chin. Phys. C Ser. **45**, 015102 (2021). https://doi.org/10.1088/1674-1137/abc066. arXiv:2006.04715
20. A.K. Ahmed, M. Azreg-Aïnou, S. Bahamonde, S. Capozziello, M. Jamil, Astrophysical flows near $f(T)$ gravity black holes. Eur. Phys. J. C Ser. **76**, 269 (2016). https://doi.org/10.1140/epjc/s10052-016-4118-5. arXiv:1602.03523
21. Event Horizon Telescope Collaboration, K. Akiyama et al., First M87 Event Horizon Telescope results. VIII. Magnetic field structure near the event horizon, Astrophys. J. Lett. **910**, L13 (2021). https://doi.org/10.3847/2041-8213/abe4de. arXiv:2105.01173
22. C. Chakraborty, Black holes shielded by magnetic fields. Phys. Lett. B Ser. **849**, 138437 (2024). https://doi.org/10.1016/j.physletb.2023.138437. arXiv:2211.11356
23. F. Atamurotov, K. Jusufi, M. Jamil, A. Abdujabbarov, M. Azreg-Aïnou, Axion-plasmon or magnetized plasma effect on an observable shadow and gravitational lensing of a Schwarzschild black hole. Phys. Rev. D Ser. **104**, 064053 (2021). https://doi.org/10.1103/PhysRevD.104.064053. arXiv:2109.08150
24. Y. Pahlavon, F. Atamurotov, K. Jusufi, M. Jamil, A. Abdujabbarov, Effect of magnetized plasma on shadow and gravitational lensing of a Reissner–Nordström black hole. Phys. Dark Univ. Ser. **45**, 101543 (2024). https://doi.org/10.1016/j.dark.2024.101543. arXiv:2406.09431
25. H. Hoshimov, O. Yunusov, F. Atamurotov, M. Jamil, A. Abdujabbarov, Weak gravitational lensing and shadow of a GUP-modified Schwarzschild black hole in the presence of plasma. Phys. Dark Univ. Ser. **43**, 101392 (2024). https://doi.org/10.1016/j.dark.2023.101392. arXiv:2312.10678
26. K. Fukumura, D. Hendry, P. Clark, F. Tombesi, M. Takahashi, Soft X-ray excess from shocked accreting plasma in active galactic nuclei. Astrophys. J. Ser. **827**, 31 (2016). https://doi.org/10.3847/0004-637X/827/1/31. arXiv:1606.01851
27. S. Mitra, D. Maity, I.K. Dihingia, S. Das, Study of general relativistic magnetohydrodynamic accretion flow around black holes. Mon. Not. R. Astron. Soc. Ser. **516**, 5092 (2022). https://doi.org/10.1093/mnras/stac2431. arXiv:2204.01412
28. F. Foucart, M. Chandra, C.F. Gammie, E. Quataert, Evolution of accretion discs around a Kerr black hole using extended magnetohydrodynamics. Mon. Not. R. Astron. Soc. Ser. **456**, 1332 (2016). https://doi.org/10.1093/mnras/stv2687. arXiv:1511.04445
29. C.M. Mobarry, R.V.E. Lovelace, Magnetohydrodynamic flows in Schwarzschild geometry. Astrophys. J. Ser. **309**, 455 (1986). https://doi.org/10.1086/164617
30. M. Takahashi, S. Nitta, Y. Tatematsu, A. Tomimatsu, Magnetohydrodynamic flows in Kerr geometry: energy extraction from black holes. Astrophys. J. Ser. **363**, 206 (1990). https://doi.org/10.1086/169331
31. C.F. Gammie, Efficiency of magnetized thin accretion disks in the Kerr metric. Astrophys. J. Ser. **522**, L57 (1999). https://doi.org/10.1086/312207. arXiv:astro-ph/9906223
32. J.D. Bekenstein, E. Oron, New conservation laws in general-relativistic magnetohydrodynamics. Phys. Rev. D Ser. **18**, 1809 (1978)
33. M. Camenzind, Centrifugally driven MHD-winds in active galactic nuclei. Astron. Astrophys. Ser. **156**, 137 (1986)
34. M. Camenzind, Hydromagnetic flows from rapidly rotating compact objects. I—Cold relativistic flows from rapid rotators. Astron. Astrophys. **162**, 32 (1986)
35. M. Camenzind, Hydromagnetic flows from rapidly rotating compact objects. II—The relativistic axisymmetric jet equilibrium. Astron. Astrophys. **184**, 341 (1987)
36. M. Takahashi, J. Goto, K. Fukumura, D. Rilett, S. Tsuruta, Standing shocks in transmagnetosonic accretion flows onto a black hole. Astrophys. J. Ser. **645**, 1408 (2006). https://doi.org/10.1086/500107. arXiv:astro-ph/0511217
37. M. Azreg-Aïnou, Cyclic and heteroclinic flows near general static spherically symmetric black holes: semi-cyclic flows addendum and corrigendum. Eur. Phys. J. C Ser. **77**, 36 (2017). https://doi.org/10.1140/epjc/s10052-017-4613-3. arXiv:1605.06063
38. H.-Y. Pu, M. Nakamura, K. Hirotani, Y. Mizuno, K. Wu, K. Asada, Steady General relativistic magnetohydrodynamic inflow/outflow solution along large-scale magnetic fields that thread a rotating black hole. Astrophys. J. Ser. **801**, 56 (2015). https://doi.org/10.1088/0004-637X/801/1/56. arXiv:1501.02112
39. S. Mitra, S. Das, Low angular momentum general relativistic magnetohydrodynamic accretion flow around rotating black holes with shocks. ApJ **971**, 28 (2024). https://doi.org/10.3847/1538-4357/ad55cb. arXiv:2405.16326
40. J. Lewandowski, Y. Ma, J. Yang, C. Zhang, Quantum Oppenheimer–Snyder and Swiss cheese models. Phys. Rev. Lett. Ser. **130**, 101501 (2023). https://doi.org/10.1103/PhysRevLett.130.101501. arXiv:2210.02253
41. S. Yang, Y.-P. Zhang, T. Zhu, L. Zhao, Y.-X. Liu, Gravitational waveforms from periodic orbits around a quantum-corrected black hole. arXiv:2407.00283